Ligand engineered bandgap stability in mixed-halide perovskite LEDs

Yasser Hassan*[1,15], Jong Hyun Park[2,15], Michael L. Crawford[3], Aditya Sadhanala[1,13,14], Jeongjae Lee[4], James C. Sadighian[3], Edoardo Mosconi[5], Ravichandran Shivanna[14], Eros Radicchi[5,11], Mingyu Jeong[6], Changduk Yang[6], Hyosung Choi[7], Sung Heum Park[8], Myoung Hoon Song[2], Filippo De Angelis[5,11,12], Cathy Y. Wong*[3,9,10], Richard H. Friend[14,] Bo Ram Lee*[8], and Henry J. Snaith*[1]

[1]Clarendon Laboratory, Department of Physics, University of Oxford, Parks Road, Oxford OX1 3PU, UK.
[2]School of Materials Science Engineering and KIST-UNIST Ulsan Center for Convergent Materials/Low Dimensional Carbon Center/Perovtronics Research Center, Ulsan National Institute of Science and Technology (UNIST), UNIST-gil 50, Ulsan, 44919, Republic of Korea.
[3]Department of Chemistry and Biochemistry, University of Oregon, Eugene, Oregon 97403, USA.
[4]School of Earth&Environmental Sciences, Seoul National University, Seoul 08826, Republic of Korea.
[5]Computational Laboratory for Hybrid/Organic Photovoltaics (CLHYO), Istituto CNR di Scienze e Tecnologie Chimiche "Giulio Natta" (CNR-SCITEC), Via Elce di Sotto 8, 06123 Perugia, Italy.
[6]Department of Energy Engineering, School of Energy and Chemical Engineering, Perovtronics Research Center, Low Dimensional Carbon Materials Center, Ulsan National Institute of Science and Technology (UNIST), 50 UNIST-gil, Ulju-gun, Ulsan 44919, Republic of Korea.
[7]Department of Chemistry, Research Institute for Convergence of Basic Sciences, Research Institute for Natural Sciences, Hanyang University, Seoul 04763, Republic of Korea.
[8]Department of Physics, Pukyong National University, 45 Yongso-ro, Nam-Gu, Busan 48513, Republic of Korea.
[9]Materials Science Institute, University of Oregon, Eugene, Oregon, 97403, United States.
[10]Oregon Center for Optical, Molecular, and Quantum Science, University of Oregon, Eugene, Oregon, 97403, USA.
[11]Department of Chemistry, Biology and Biotechnology, University of Perugia, Via Elce di Sotto 8, 06123 Perugia, Italy.
[12]CompuNet, Istituto Italiano di Tecnologia, Via Morego 30, 16163 Genova, Italy.
[13]Centre for Nano Science and Engineering, Indian Institute of Science, Bangalore 560012, India.
[14]Cavendish Laboratory, University of Cambridge, J J Thomson Avenue, Cambridge CB3 0HE, UK.
[15]These authors contributed equally: Yasser Hassan, Jong Hyun Park.

Lead halide perovskites are promising semiconductors for light-emitting applications, owing to their bright, bandgap tuneable, and high colour purity luminescence[1,2]. Close to unity photoluminescence quantum yields have been achieved for perovskite nanocrystals across a broad range of emission colours, and light-emitting diodes with external quantum efficiencies exceeding 20%, which approach commercial OLEDs, have been demonstrated in both the Infrared and green emission channels[1,3,4]. However, due to the formation of lower bandgap iodide-rich domains in mixed-halide perovskites, achieving colour-stable and efficient red electroluminescence has not been realised[5,6]. Here, we report mixed-halide perovskite nanocrystals treated with multidentate ligands that suppress halide segregation under electroluminescent operation. We demonstrate colour-stable red emission centred at 620 nm, with electroluminescence external quantum efficiencies of 20.3% in light-emitting diodes. We show that a key function of the ligand treatment is to "clean" the nanocrystal surface through the removal of lead atoms, and via density functional theory, we find the nature of binding between the ligands and the nanocrystal surface suppresses iodine Frenkel defect formation, which inhibits halide-segregation. Our work exemplifies how the functionality of metal halide perovskites is extremely sensitive to the nature of the (nano)crystalline surface and presents a route for controlling surface defect formation and migration. This is critical for achieving

band gap stability for light emission and may also have a broader impact for other optoelectronic applications, such as photovoltaics, where bandgap stability is required.

The bandgap, and hence emission wavelength, of metal halide perovskites, can be tuned by several means, such as quantum confinement[7-10] in nanocrystals (NCs)[5,6] and two-dimensional perovskites[11-14], or by varying the halide composition in the ABX_3 perovskite stoichiometry, where A is organic ammonium or alkaline metal cation, B is a group IV metal cation, typically lead, and X are halide anions[5,6,15-17]. A red emission wavelength between 615 and 640 nm, required for displays, can be obtained with photoluminescence quantum yields (PLQY) approaching unity using a mixture of iodide and bromide NCs[5,6,15,16]. However, these NCs are susceptible to halide segregation upon photoexcitation and the application of electrical bias[5,18-20]. Despite much effort, colour-stable red electroluminescence (EL) from mixed halide perovskite NCs has not yet been realised[5,11-15,17,21-28].

Recent investigations suggest halide segregation occurs via diffusion of vacancy and interstitial defects[18,19]. In mixed-halide perovskite films measured experimentally and neat-I systems studied computationally, halide defects appear to migrate to grain boundaries or crystal surfaces[29-34]. For polycrystalline films, improvements in bandgap stability and device efficiency have been achieved by passivating grain boundaries with alkali metal halides or larger organic ammonium cations[7,8,11,17,27,35]. For NCs, this is particularly critical due to the high surface area to volume ratio and reports that halide segregation can occur both within (intra) and between (inter) NCs[20,36]. An approach to solving the halide segregation issue in NCs may lie in discovering a surface treatment that removes or immobilises surface defects[5,15].

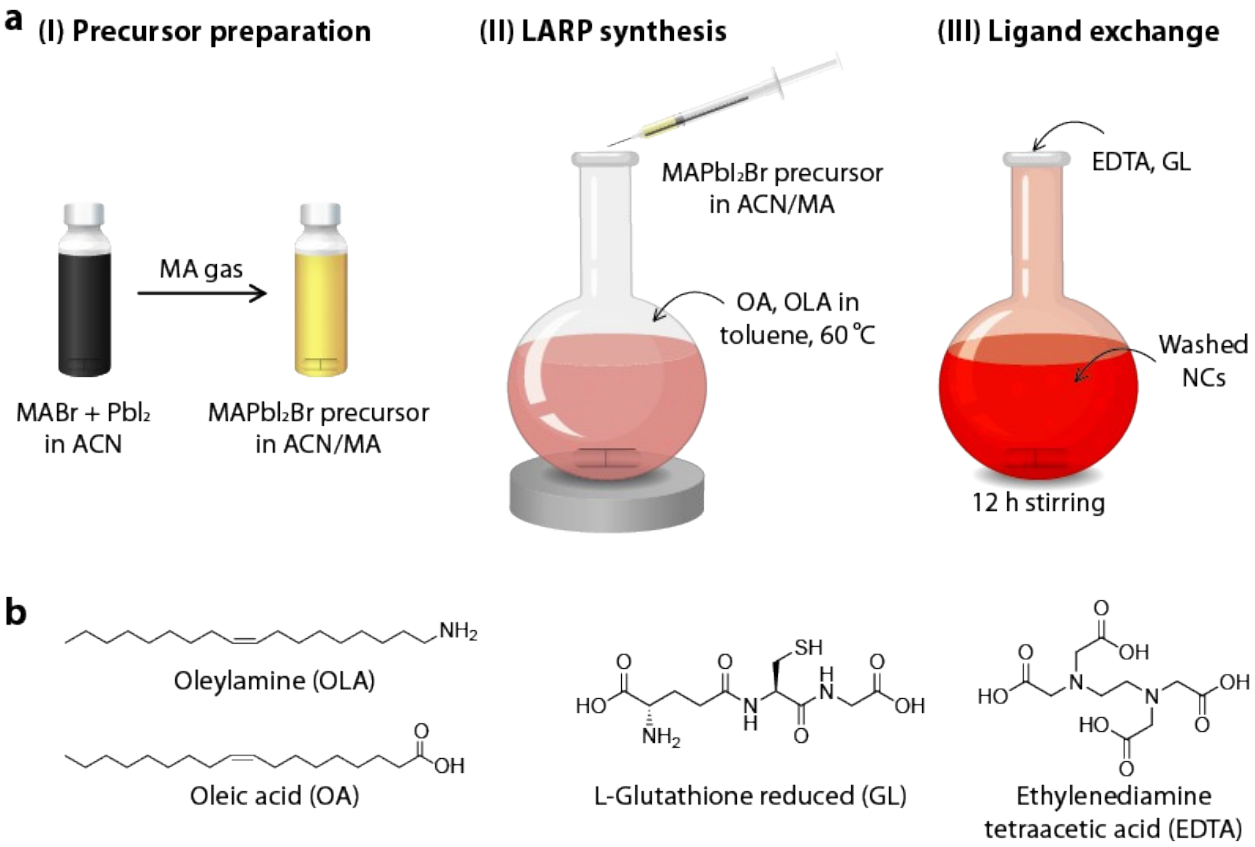

Figure 1. Illustration of NC synthesis. a, Synthesis and ligand treatment steps: (i) Dissolution of perovskite precursors in acetonitrile (ACN) and methylamine (MA), (ii) NC synthesis by modified LARP, and (iii) post-synthetic ligand treatment. **b**, chemical structures of ligands used.

We synthesised $CH_3NH_3Pb(I_xBr_{1-x})_3$ NCs *via* a modified ligand-assisted re-precipitation (LARP) method[5]. Following purification, we performed a ligand treatment with ethylenediaminetetraacetic acid (EDTA) and L-glutathione reduced (GL) (**Fig. 1**). These molecules bind strongly to lead in biological systems[37-40]. To assess the impact of the ligand treatment, we performed photoluminescence (PL), PLQY, attenuated total reflection Fourier transform infrared spectroscopy (ATR-FTIR), X-ray photoelectron spectroscopy (XPS), and X-ray diffraction (XRD) measurements, which we show in **Fig. 2**, and **(Extended Data Fig. 1)**.

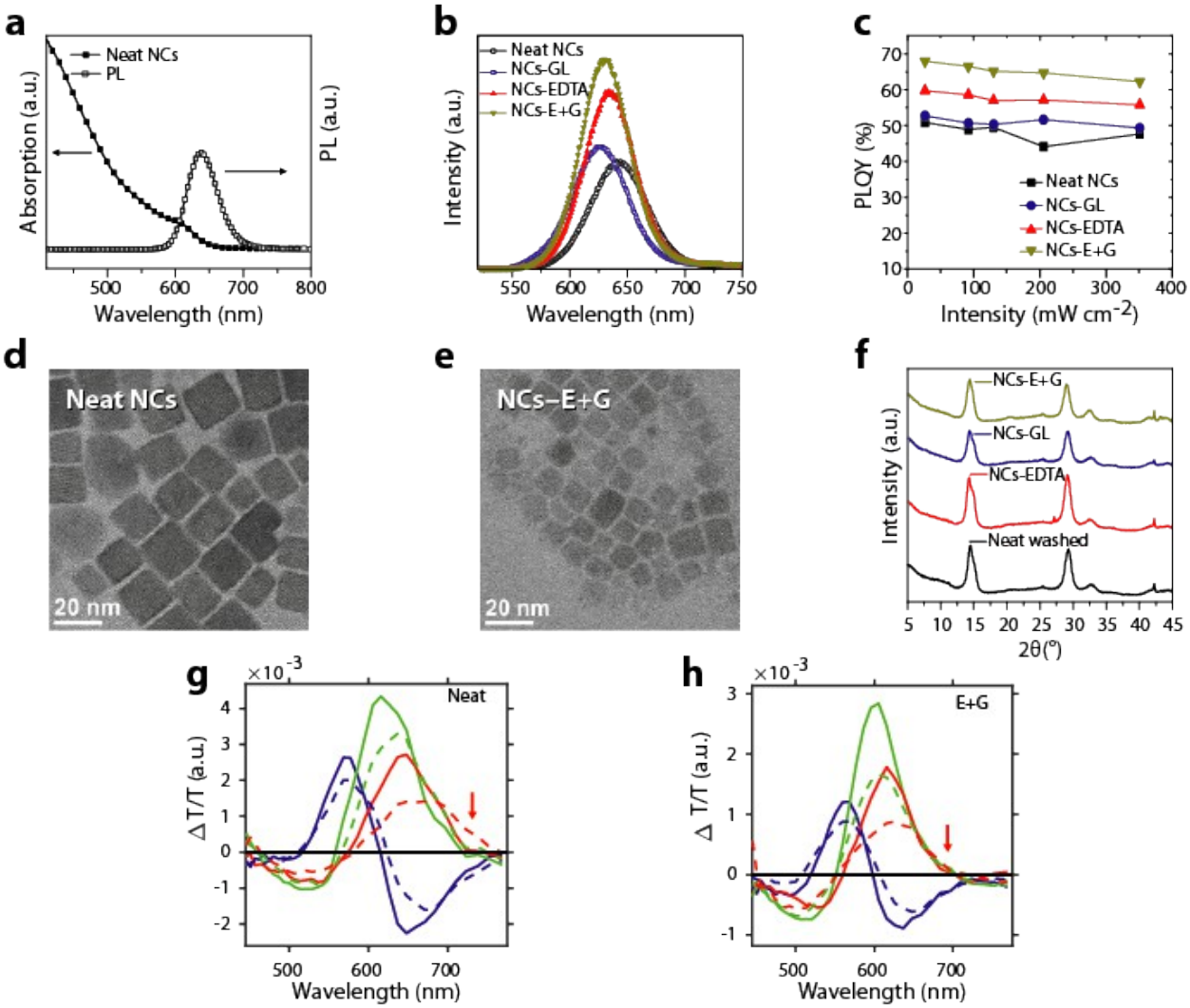

Fig. 2. Impact of ligand treatment on the solution photoluminescence and NC structural properties. **a,** Absorption and PL spectra of as-synthesised $MAPb(I_{1-x}Br_x)_3$ NCs in solution. **b,** PL spectra of NC films following post-synthetic treatment with GL, EDTA, and EDTA + GL (E+G). **c,** Excitation fluence dependence of PLQE of NC thin films before and after ligand treatment, measured in an integrating sphere. **d,e**, High-resolution transmission electron micrograph (HR-TEM) image for NCs before and after ligand treatment with E+G, respectively. **f,** XRD for the NCs films before and after ligand treatment. **g,h**, Decay associated difference spectra from a global fit of TAS measurements of neat- and E+G-capped NCs, respectively. Solid and dashed lines are spectra before and after 30 s of exposure to a 7.1 W cm^{-2} 405 nm CW laser. Blue, green, and red traces correspond to decay components with time constants of ~400 fs, ~14 ps, and ~280 ps, respectively. Red arrows indicate the red edge of the spectra, where changes in the bandgap of the material would result in changes to the bleaching of the sample due to band filling.

As-synthesised $MAPb(I_xBr_{1-x})_3$ NCs in toluene exhibit PL centred at 642 nm **(Fig. 2a)**. After ligand treatment with GL, we observe an increase in intensity and a blue-shift in the PL peak position to 625 nm, **Fig. 2b**. We observe an increased PL intensity and only slight blue-shift to 635 nm if EDTA is used instead. Using an equimolar mixture of EDTA and GL (denoted E+G), we observe emission at 630 nm and an overall increase in PL intensity, **Fig. 2b**. PLQY measurements of NC thin films confirm that the ligand treatment decreases the total number of active defects, **Fig. 2c**. These data are consistent with E+G treatment being most favourable for suppressing non-radiative recombination. High-resolution transmission electron microscopy (HR-TEM) shows size reduction of the E+G NCs compared to neat NCs (average cubic dimensions of 12 ± 1.7 nm versus 16.3 ±2 nm, respectively, **Fig. 2d,e** and **Extended Data Fig. 2**). Exciton energy is linearly dependent on the inverse square of NC size for weakly-confined excitons. A blue-shift in emission, consistent with quantum confinement and lattice relaxation, has been measured for perovskite nanoparticles within this size range[41]. Furthermore, we have previously observed up to an 80 nm blue-shift in emission due to size confinement effects in similarly sized $MAPbI_3$ NCs[5]. We hence expect size reduction due to ligand treatment to increases quantum confinement, contributing to the observed blue-shift in emission[41].

Employing XPS (**Extended Data Fig.1)**, we find the I:Br ratio changes from 2:1 in the precursor solution to approximately 2:3 in synthesised NCs. We expect a bulk emission at 647 to 655 nm for this composition. Following ligand treatment, we determine a minor enrichment in bromide content, which would account for up to 8nm blue shift in emission for the E+G sample[42]. We also expect a change in lattice constant of ~0.019 Å per 10 nm shift in PL peak position for changing halide compositions in polycrystalline $MAPb(I_{1-x}Br_x)_3$

films[42], however, XRD measurements reveal a cubic lattice constant of 6.05 Å for NC films both before and after ligand treatment (**Fig 2f**). Collectively, these results suggest that both compositional changes and confinement effects are influencing the emission peak position.

To assess if the ligand treatment suppresses halide segregation and improves bandgap stability, we performed transient absorption spectroscopy (TAS), **Extended Data Fig. 3**. We measured NC films with and without the E+G ligand treatment, as prepared and after exposure to a 405 nm laser. A global fit of the signal yields decay associated difference spectra (DADS), **Fig. 2g,h**. The sub-ps TAS decay arises from bandgap renormalisation, Auger recombination, and carrier cooling[43]. Carriers accumulate near the band edge, causing optical bleaching at these energies. The longest TAS decay originates from carrier recombination. After irradiation for 30 s, TAS spectra for the neat sample display a new low energy bleach, visible in the longest DADS component. In contrast, the DADS line-shape for the E+G treated sample remains approximately unchanged after irradiation. The emergence of the low energy bleach in the neat sample is consistent with lower bandgap iodide-rich minority phases emerging, from which charge carriers recombine, which is hence suppressed in the E+G treated sample.

Segregation between NCs necessitates the creation of Br-rich and I-rich NCs. This has been observed in other perovskite NCs and results in the presence of a second, higher energy PL emission in addition to the red-shifted PL[20,36]. In **Extended Data Fig. 4** we show that even at very low NC concentrations in a polymer matrix we observe a red-shifted emission, with no growth of a high energy peak nor broadening of the high energy emission shoulder following irradiation. Confocal PL measurements on such films reveal a red-shifted emission under

137 illumination from what appear to be single NCs. The lack of a high energy feature in the TAS
138 spectra of illuminated neat NCs also indicates that Br-rich NCs are not forming, suggesting that
139 segregation can occur within individual NCs.

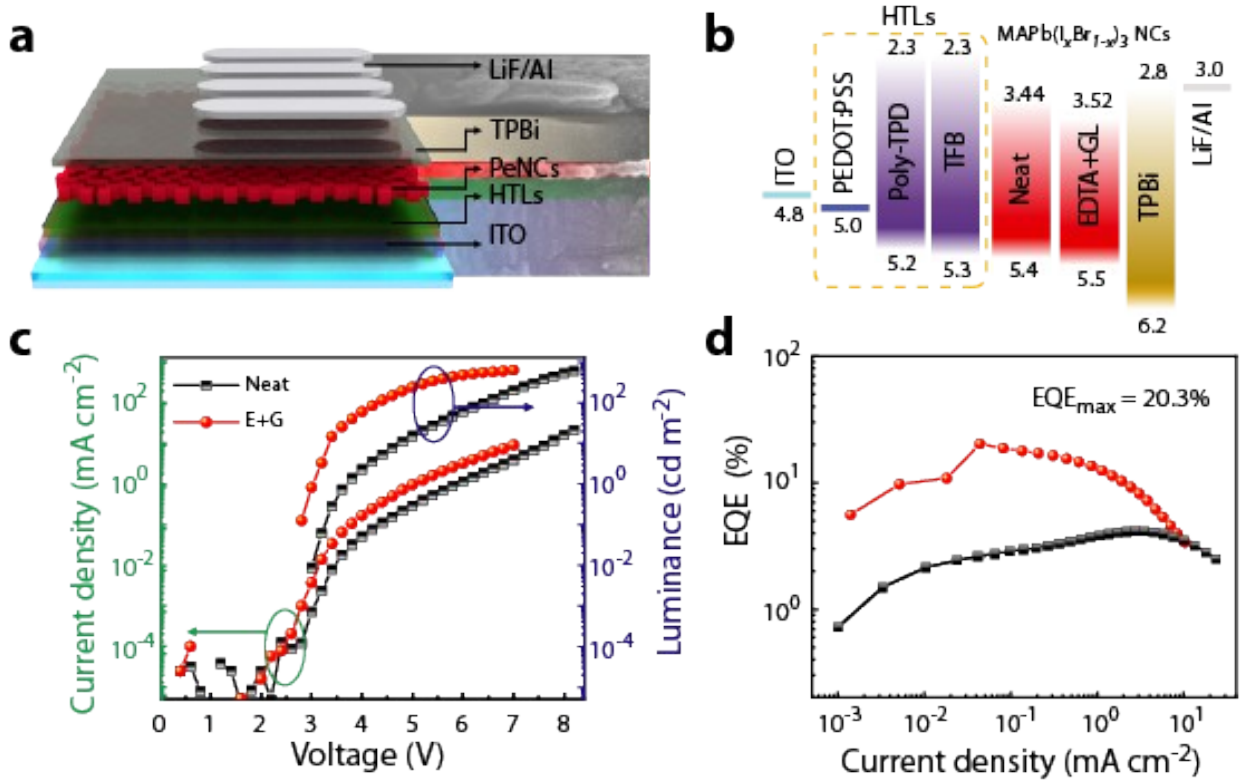

e

Device configuration	LE_{max} [cd m^{-2}] @ bias (V)	LE_{max} [cd A^{-1}] @ bias (V)	EQE_{max} [%] @ bias (V)	Turn-on Voltage [V] @ 0.1cd m^{-2}
Neat PeNCs-LED	598 @ 8.2	4.53 @ 6.4	4.13 @ 6.6	3.2
E+G PeNCs-LED	627 @ 7.0	31.28 @ 3.4	20.28 @ 3.4	2.8

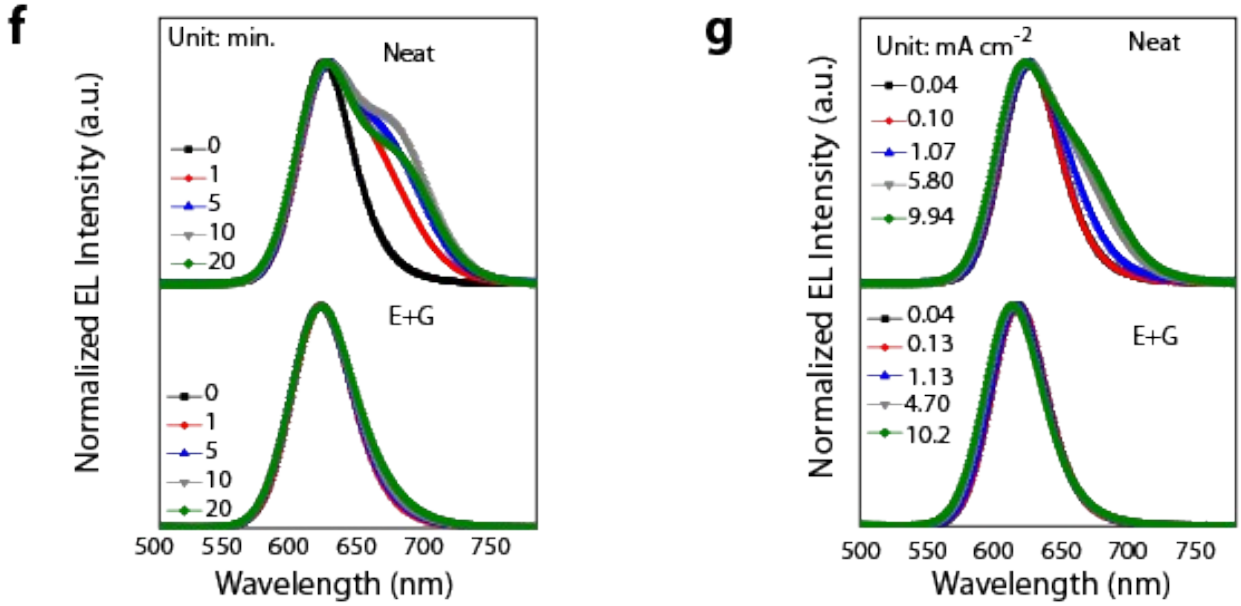

140

Figure 3. Device characterisation of mixed halide $MAPb(I_{1-x}Br_x)_3$ NC-LEDs: a, Schematic illustration of $MAPb(I_{1-x}Br_x)_3$ NC-LED architecture and scanning electron microscopy (SEM) image showing the cross section of a device; thickness of each layer is confirmed by SEM image: PEDOT:PSS/Poly-TPD/TFB HTLs (30 nm), NC emission layer (20 nm), TPBi ETL (70 nm), LiF/Al electrode (80 nm). **b,** Energy band diagram of the materials employed in these LEDs, from references[44-46]. Operational characteristics for LEDs incorporating neat and E+G ligand treated NC layers; **c,** Current density–voltage and luminance(L)-voltage curves, **d,** EQE-current density curves, **e,** device performance parameters of best-performing LEDs (LE is luminous efficiency)**. f,** EL spectra at different time intervals for LEDs held at a constant current density of 1.5 mA cm^{-2} **g,** EL spectra at different current densities (mA cm^{-2}).

We next assess the impact of the ligand treatment upon NC-LEDs. We find that both EDTA and GL significantly suppress the halide segregation and improve bandgap stability, but EDTA treated NC-LEDs exhibit a small broadening in the EL FWHM during operation. On the other hand, GL treated NC-LEDs show the most stable emission spectra but lower device efficiency. Efficient and colour-stable NC-LEDs were achieved with the E+G treatment (**Extended Data Fig. 5**). To better understand the role of each ligand, we ran a second ligand treatment step using a soft Lewis base of adamantane carboxylic acid (ADAC) and constructed LEDs. EDTA, GL, and E+G treated NC-LEDs show a negligible peak shift and small FWHM broadening during operation. However, EDTA and E+G treated NCs, which are treated with ADAC show a more significant peak shift and broadening. In contrast, GL treated NC-LEDs show stable EL, even after the ADAC treatment. These observations indicate that GL is more strongly bound to the NC surface than EDTA, but EDTA appears to be important for achieving the highest efficiencies.

When choosing charge injection layers and optimising the performance of the LEDs, we found that maximising the PLQY of the half-constructed devices led to a rapid and effective selection of ideal materials. We show the results of such studies in **Extended Data Fig. 6–7**. Our final device stack, together with a schematic and a

scanning electron microscopy (SEM) cross-sectional image, is shown in **Fig. 3a and b**. We observe higher current densities in E+G NC-LEDs, and significantly improved EQEs (**Fig. 3c,d)**. We measured a peak EQE of 20.3% at ~0.1 $mAcm^{-2}$ current density and ~620 nm emission wavelength. This places red perovskite LEDs in the same quantum efficiency range as commercial OLEDs. Considering the PLQY of the isolated perovskite NC films, the refractive indices of the materials, optical outcoupling, and photon recycling, we estimate a maximum feasible EQE of 32.4%,[47,48] discussed in **Methods**. This indicates that there remains potential for further improvement through improved device design.

The most pressing challenge for red-emitting metal halide perovskites is achieving band gap stability. In **Fig. 3f,g**, we show the emission spectra for LEDs operating at a fixed current density over time and over a range of current densities, respectively. For the neat NC-LEDs held at a constant current density of 1.5 $mAcm^{-2}$ (and 10 $mAcm^{-2}$ shown in **Extended Data Fig. 8**) measured over 20 minutes, we observe a broadening of the emission peak and the emergence of a shoulder at ~680 nm. We observe a similar broadening and the emergence of a shoulder when the neat NC-LEDs are measured at increasing current densities. These observations are consistent with halide segregation driven by electrical biasing/current injection during LED operation and causing lower energy emission from iodide enriched regions. In contrast, the emission spectrum for the E+G NC-LEDs is stable at 620 nm under the same operating conditions and duration. We note, however, that the absolute EL intensity decays over time. **Extended Data Fig. 8** shows the luminance as a function of time for E+G NC-LEDs held at current densities of 0.1, 1, and 10 mA^{-2}. The time to 50% of initial luminance (T_{50}) decreased from 340, to 130, to 16 minutes, respectively. Therefore,

although we have achieved colour-stable red emission, the challenge to deliver long-term stability in absolute brightness and efficiency remains.

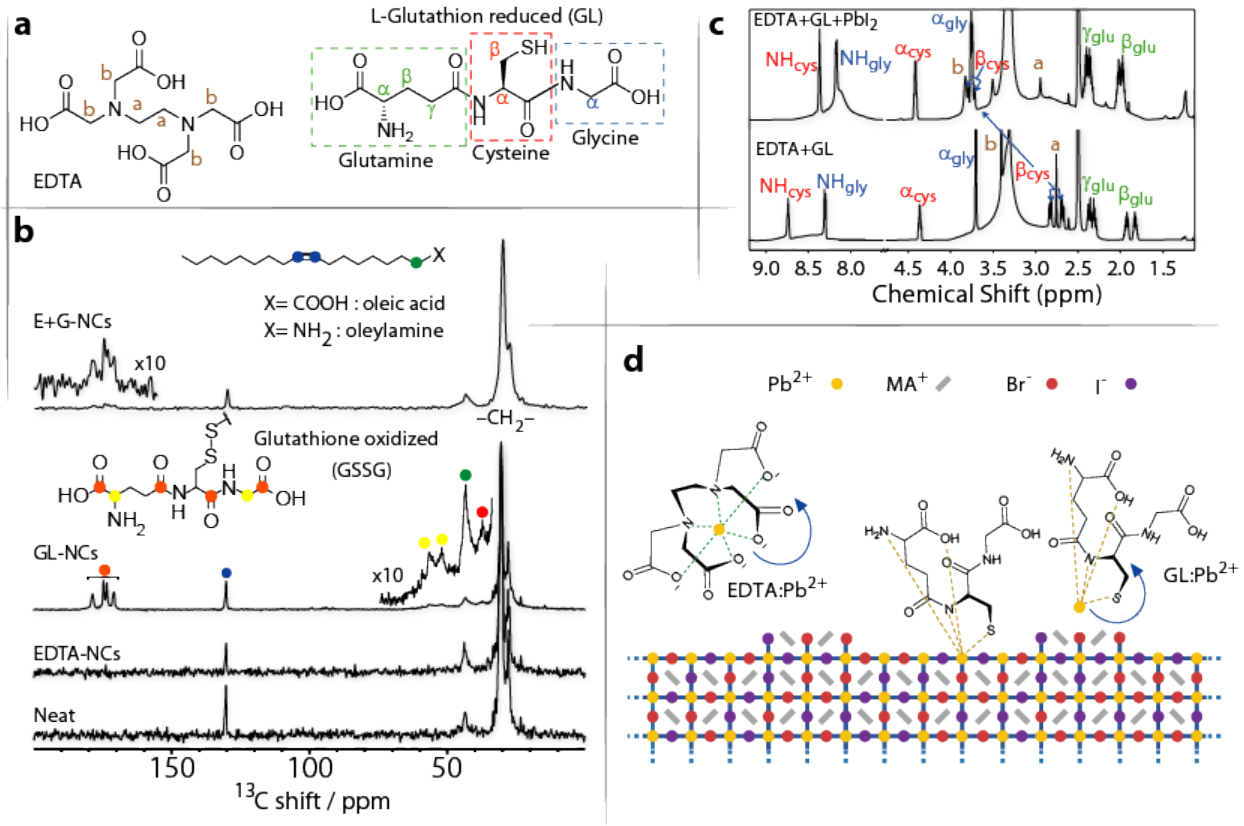

Figure 4. a, ^{13}C solid-state NMR spectra of neat and ligand (GL, EDTA, E+G) treated NCs. Insets show ligand structure. **b**, Molecular structure of EDTA and GL. Peaks a and b are characteristic of CH_2 as labelled in the molecular structure of EDTA while peaks α, β, and γ are characteristic of CH_2 in GL. **c,** Solution ^{1}H NMR spectra of E+G with and without PbI_2 in d-DMSO solutions. **d,** Proposed molecular interactions of GL and EDTA with Pb^{2+} atoms on the NC surface.

Understanding the origin of this improved device performance requires identifying the key ligand-perovskite interactions that stabilise the surface. To this end, we performed solid-state ^{13}C NMR of the OA/OLA-capped NCs before and after the E+G treatment. The resulting data, **Fig. 4a**, show a clear peak at 130.2 ppm (blue dot), which arises from the double-bonded carbons in the OA/OLA molecules. The presence of this peak, alongside the aliphatic -CH_2- peaks (30-27 ppm), clearly signifies the existence of OA/OLA on the NC surface even after the EDTA, GL or

E+G ligand treatment; these remaining nonpolar OA/OLA chains are likely to ensure NC solubility in toluene even after the ligand treatment. The absence of EDTA peaks from the EDTA-treated sample shows that the amount of EDTA on the NC surface is below the detection limit of NMR, while clear GL peaks arising from the carbonyl (orange) and α-carbonyl (yellow) environments confirm their presence. The peak at 38 ppm (red dot), **Fig 4a**, suggests the presence of oxidised GL, which may indicate that reduction of some species on the perovskite surface could serve as a part of the active role of GL, although this remains speculative at this stage. A key function of GL and EDTA ligands can be inferred from their Pb binding ability: both EDTA and GL are known to bind strongly to Pb atoms, shown through solution-state NMR (**Fig. 4c** and **Extended Data Fig. 9**, details in **Method**).

We show the proposed molecular interactions of the E+G ligands with Pb^{2+} on the NC surface in **Fig. 4d**. We postulate that part of the role of EDTA and GL is to remove undercoordinated lead from the NC surface, resulting in an electronically "cleaner", less defective surface. This "stripping" action is consistent with (i) reduction in NC sizes, (ii) existence of Pb-ligand complexes in solution, and (iii) large binding energy of EDTA and GL to Pb atoms (**Extended Data Fig. 10**). We note that some of the excess ligands in the treatment may then bind to the remaining Pb on the "cleaned" perovskite surface, further decreasing the defect concentration.

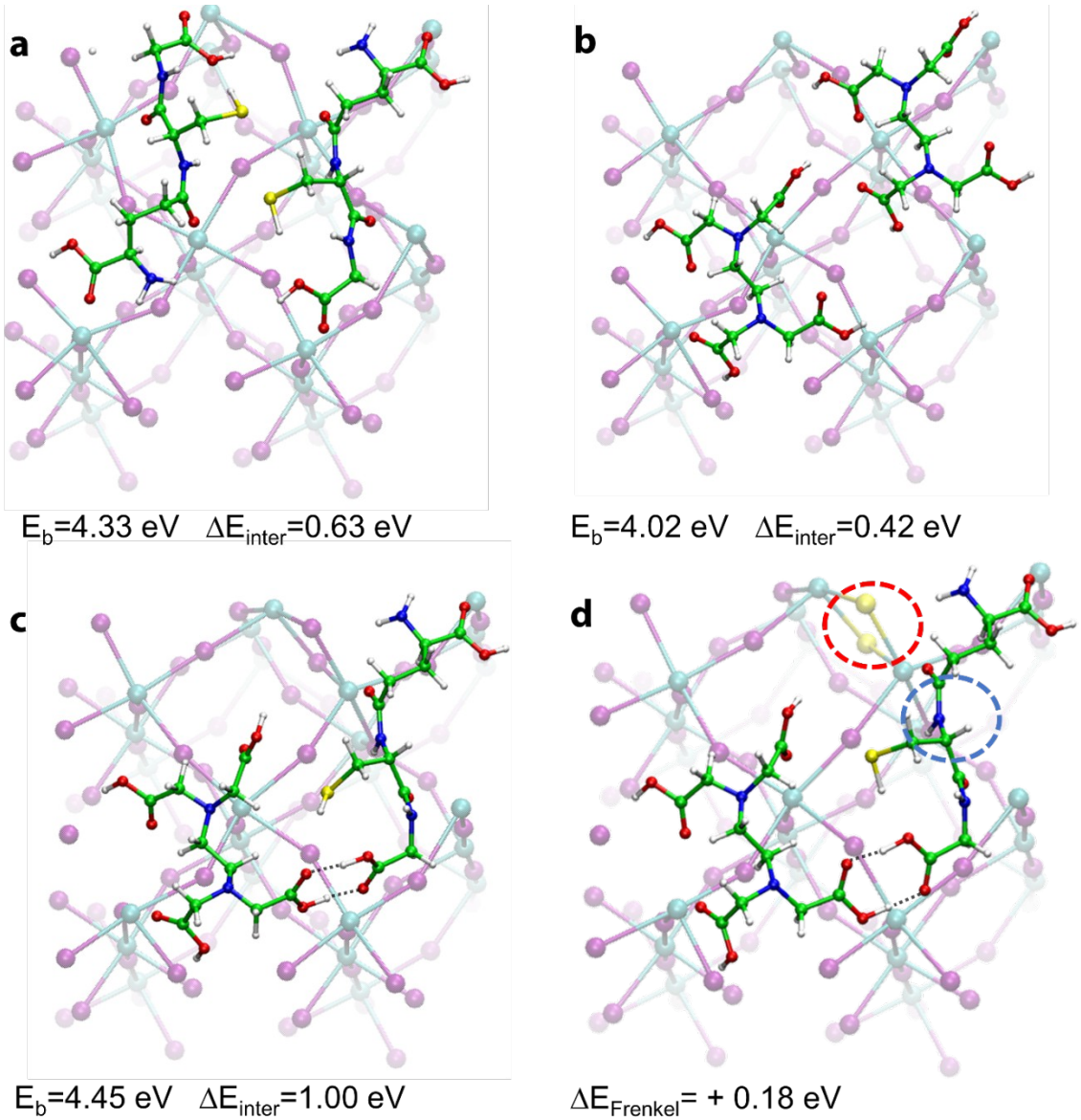

Figure 5. Optimised structures of two interacting surface adsorbed **a,** GL, **b,** EDTA, and **c,** one GL and one EDTA molecule, along with calculated total biding energies (E_b) and their intermolecular contribution (ΔE_{inter}) in eV calculated with respect to the isolated surface adsorbed molecules (E_b=1.85 and 1.60 eV for GL and EDTA, respectively). **d,** Optimised structure of an iodine Frenkel defect pair – defective sites highlighted by red and blue circles - in the presence of adsorbed GL+EDTA along with the increase of defect formation energy compared to the unpassivated surface ($\Delta E_{Frenkel}$, in eV).

To gain further understanding of ligand binding, we use DFT to model the interaction of GL and EDTA with the surface of $MAPbI_3$ **(Fig. 5)**. We consider a PbI_2-terminated surface representative of a completely unpassivated perovskite surface with exposed, undercoordinated

Pb atoms. We decomposed GL and EDTA into their possible binding moieties and calculated the binding energy (BE) of each ligand to the perovskite surface **(Extended Data Fig. 10)**. The binding energy is defined as BE = $E_{lig@surface} - E_{lig} - E_{surface}$, where the latter three terms are the energy of the surface and bound ligand, the energy of the isolated ligand, and the energy of the bare surface, respectively. Our calculated BE for GL is -1.85 eV, which is large compared to the calculated value of -0.58 eV for acetic acid or -0.84 eV for methylamine, representative of carboxylic acid and primary amine binding moieties of GL. We deduce that the large BE is due to contributions from multiple binding moieties. We also determine a large BE for EDTA (-1.60 eV), slightly lower than that of GL, with steric hindrance limiting binding from the tertiary aminic group; this is also consistent with the observation of only GL in the ^{13}C solid-state NMR spectra of E+G NCs **(Fig. 4a)**.

We further evaluate the BE of two interacting GL molecules, two interacting EDTA molecules, and an interacting E+G pair of molecules on the perovskite surface **(Fig. 5, Extended Data Fig. 10)**. The E+G pair has the highest binding energy, enhanced by a synergistic effect between GL and EDTA; intermolecular hydrogen bonding between carboxylic groups of GL and EDTA provides extra stabilisation to these surface adsorbed molecules, leading to a BE of -4.45 eV **(Extended Data Fig. 10)**.

Our calculations confirm that this specific pairing of ligands leads to a strong affinity with the perovskite surface. We now assess how this influences the migration of halide species. Iodine Frenkel defects, which are iodide interstitial-vacancy pairs, are the most energetically probable defects at the PbI_2-terminated perovskite surface, with shallow formation energy (0.03 eV). We calculate the formation energy of an iodine Frenkel defect at the PbI_2-terminated perovskite

surface in the presence of GL, E+G, or without passivating molecules, details in **Methods**. We find that GL surface passivation raises the iodine Frenkel defect formation energy to 0.15 eV, while E+G further increases the formation energy to 0.18 eV. This is significantly higher than calculated values for other passivating agents, for example, in the presence of polyethylene oxide, the formation of an interstitial iodine defect becomes less favourable by 0.08 eV, compared to bare perovskite surface.[32] To summarise, the high calculated binding energy, coupled with the significant increase in the iodide Frenkel defect formation energy, suggests that the GL and the combination of E+G ligands significantly inhibits undercoordinated Pb atoms from stabilising these Frenkel defects[49]. Since halide Frenkel defects are expected to be the ionic species responsible for halide segregation under illumination or device operation, our results are consistent with suppressed defect formation suppressing halide segregation in E+G treated NCs.

In conclusion, we have demonstrated that a lead-complexing multidentate ligand treatment leads to bandgap stable red electroluminescence from mixed halide perovskite NC-LEDs, with a peak EQE at 620 nm surpassing 20%. We have found that stripping the NC surface of defects is part of the active role of the ligands. Furthermore, we have shown that both ligand-ligand and ligand-surface interactions are important for achieving a stable ligand shell on the NC surface, and the multidentate ligand interactions with the surface greatly suppress surface defect formation. Beyond light emission, our work here is likely to be broadly applicable to stabilising the bandgap of mixed-ion metal halide perovskites for a range of applications, including multi-junction photovoltaics, and will enable perovskites to deliver upon the promise of being remarkably versatile and tuneable semiconductors.

Methods

All NC syntheses were carried out at ambient conditions in a fume hood.

Materials

All chemicals were used as received without further purification. Lead iodide (PbI_2) (99.99 %) was purchased from TCI Chemicals; methylammonium iodide (MAI) and methylammonium bromide (MABr) from Dyesol; oleic acid (99.0 %), oleylamine (70 %), methylamine (MA) solution (33% in absolute ethanol), ethylenediaminetetraacetic acid (anhydrous, ≥99%), and L-glutathione reduced (≥98.0%) from Sigma-Aldrich. All solvents such as toluene, acetonitrile, and methyl acetate were anhydrous and were purchased from Sigma-Aldrich. PEDOT:PSS (AI 4083), Poly-TPD, and TPBi were purchased from OSM. TFB was purchased from Ossila.

Preparation of Lead Mixed Halide Perovskite Precursor

Typically, a perovskite precursor solution was prepared according to our recent work (ref 5), where 922 mg of PbI_2 and 223 mg of MABr were mixed with 4 mL of acetonitrile (ACN) and shaken to form a green-black suspension. Dry CH_3NH_3 (MA) gas was bubbled through the suspension to form a compound solvent, hereafter referred to as ACN/MA, detailed elsewhere [(ref 5)].

Synthesis of $MAPb(I_{1-x}Br_x)_3$ Perovskite NCs for Red Emission

The synthesis of the $MAPb(I_{1-x}Br_x)_3$ NCs was carried out by injecting 0.2 mL of perovskite precursor dissolved in ACN/MA into ~60 $^{\circ}$C toluene containing 2 mL of OA and 0.2 mL OLA. The NCs immediately nucleated, turning the suspension red. The reaction was continued for 1-2 min to allow for crystal growth before the NC suspension was immersed into an ice bath. We

synthesised six batches of NCs simultaneously, collected them into three centrifuge tubes (each containing 10 mL of NCs), and the NCs were iteratively precipitated by adding 20 mL of anhydrous methyl acetate. The NCs were separated from excess unreacted ligands/precursors and purified by centrifugation at 8,000 rpm for 10 min, then re-dispersed into 5 mL toluene. We added 10 mL methyl acetate to each tube and repeated the purification process before the NCs were re-dissolved in toluene to a concentration of 40 mg mL^{-1} for further characterisation. These purified NCs, capped with OA and OLA, are denoted as "neat NCs." These neat NCs exhibit PL at 630 nm, and their tetragonal phase was confirmed by powder X-ray diffraction (PXRD), **Fig. 2f**.

Ligand Treatment of $MAPb(I_{1-x}Br_x)_3$ Perovskite NCs

The NCs underwent two washing cycles with a methyl acetate mixture, as described above. Each NC batch was dispersed in 2 mL of toluene after the washing process. Six batches of washed NCs were combined to make a 12 mL (40 mg mL^{-1}) stock solution. This solution was centrifuged another time at 5,000 rpm for 5 minutes to remove aggregates and large particles. The collected supernatant was divided into two portions: one was used as the control neat sample, while the other was treated by a new ligand. Typically, 2 mmol of ligand was added to 3 mL of NCs in toluene and stirred overnight (~12 hrs) at room temperature. The unreacted ligand powder was separated from the NCs after ligand treatment by centrifugation at 8,000 rpm for 10 min. The collected supernatant was filtered using a PTFE syringe filter (Whatman, 0.2 µm) and stored for further characterisation and device work.

Transient Absorption Spectroscopy of $MAPb(I_{1-x}Br_x)_3$ NCs

A Ti:Sapphire laser (Coherent Astrella) operating at 1 kHz pumped an optical parametric amplifier (Light Conversion, Topas Prime Plus) to generate 520 nm pump pulses. The 800 nm fundamental was used to generate white light probe pulses in a sapphire plate. The TAS pump pulse energy was 106 μJ cm^{-2}. The broadband probe pulse energies were 124 μJ cm^{-2} and 146 μJ cm^{-2} for the E+G and C films, respectively. Transient absorption spectroscopy (TAS) spectra were collected using a homebuilt instrument with 100 fs time resolution and pump-probe time delays of up to 800 ps. The TAS signal at alternate time delays was collected in ascending order, and the signal at the remaining time delays in descending order, to ensure that any changes in the sample during the scan were not systematically encoded into the transient. Each scan required 50 s. 72 TAS spectra for each film were measured prior to 30 s of exposure to a 405 nm CW laser with the power density set at 7.09 W cm^{-2}. The 405 nm laser also acted as the excitation source for the measurement of fluorescence spectra. Fluorescence was collected through a fibre optic cable (Thorlabs M53L01) by a portable spectrometer (Ocean Optics, Flame-T). After completing the exposure, the TAS instrument was initialised, a process that requires 40 s. TAS scans were then collected, with a few seconds of exposure to the 405 nm CW laser before and after each scan to compensate for the recovery of the halide migration during the TAS scan. This procedure was repeated for 60 TAS scans, **Extended Data Fig. 3**.

Absorbance, fluorescence, and TAS measurements were performed on OA/OLA- and EG-capped NCs in spin-cast encapsulated films. The average wavelength of the fluorescence immediately before and after each TAS scan was used to estimate the average fluorescence wavelength during the scan. This estimates the average amount of halide segregation over 60 TAS scans. The duration of exposure to the 405 nm light after each scan was set to minimise the change in the

average fluorescence wavelength during the 60 TAS scans, shown in **Extended Data Fig. 3**. TAS measurements were performed on different spots on each film using different durations of 405 nm exposure between TAS scans until a small standard deviation in the average fluorescence wavelength was achieved. This indicated that, with this additional irradiation, the NCs were not continuing to undergo further halide segregation nor recovery of segregation during the 60 TAS scans.

Calculation of the EQE-EL Limit

Our observed EQE-EL of more than 20% appears to be at the limit of what is feasible when considering optical outcoupling efficiencies from perovskite thin films in LED device structures[50]. However, the precise outcoupling efficiency depends strongly upon the refractive index of the emission layer, and furthermore, photon recycling can contribute to enabling waveguided light to be reabsorbed and externally emitted from the device. In order to quantify this is in more detail, we firstly estimated the refractive index of our nanocrystal films using spectroscopic ellipsometry and estimate an n = ~1.82 @ 620nm. Considering a thin film on glass, with an n = 1.82, and accounting for emission from both the perovskite/air and perovskite/glass interfaces, we determine an outcoupling efficiency of 32.4%. Our observations of a PLQY of 70% for such films is clearly in excess of this, but can be understood by accounting for photon recycling, following the procedure of Richter *et. al* [51]. For our films, with an outcoupling efficiency of 32.4% and an external PLQY of 70%, we estimate an internal PLQY of 87.6% (We show further details of this calculation below). For the LEDs, this calculation is slightly more complicated since there are a larger number of material layers, there is a reflective rear electrode, and parasitic absorption can occur in the charge injection layers and electrode materials[52]. However, detailed

366 calculations have been made for organic light-emitting diodes with very similar device stacks
367 and refractive indices for the materials used, including the emission layer at n~1.8. Putting out
368 internal PLQY of 87.8% into the calculated escape cone efficiencies of Salehi *et. al*[53] results in an
369 estimated EQE for EL of 32.4%. Therefore, our measured EQE-EL of 20% is entirely feasible, and
370 there yet remains a capacity for further improvement.

371 **Details of the internal PLQY calculation [Ref 51]:**

372 Here we measure the PLQY of a perovskite film coated upon a glass slide measured in an
373 integrated sphere. The light will be isotopically emitted within the perovskite film, and a certain
374 fraction emitted within a specific solid-angle will escape from the front and back surface of the
375 film, with a considerable fraction of the light totally internally reflected and reabsorbed in the
376 plane of the film. Since the overlap of emission and absorption spectra are significant for these
377 perovskite materials, we estimate that within a few tens of microns, more than 90% of the
378 waveguided light will be reabsorbed and hence very little light will be emitted from the edges of
379 perovskite film coated on the 2 × 2cm glass slides. The analysis which we set out below, which
380 includes realistic parameters, determines the relationship between measured PLQE and internal
381 PLQE. The probability for a photon isotopically emitted from within one medium, to be
382 transmitted through an interface between the medium within which it was emitted and the
383 adjacent medium, with refractive indices and respectively, can be estimated as
384

where Ω_{esc} is the escape solid angle, and T is the transmittance. An ellipsometry measurement estimates the refractive index of perovskite NC films to be ~1.82 @ 620 nm. Taking the refractive index of air, glass, and the perovskite NC film to be 1, 1.5, and 1.82 respectively, we estimate the transmission probability of a photon from the above equation for the perovskite-air interface to be 6.9 % and the perovskite-glass interface to be 16.8 %.

We assume the optical density of the NC films to be 0.02 at the PL emission wavelength of 620 nm (or 2 eV). Before reaching an interface, photons will, on average, have travelled through an optical density of 0.01. Of the total photons emitted, 16.8% of the photons will be traveling towards the perovskite/glass interface within the escape cone, and 6.9% of the photons will be traveling towards the perovskite/air interface within the escape cone. The photons emitted towards the perovskite/air interface, but within the solid-angle in between the perovskite/air and perovskite/glass escape cones (which accounts for 16.8%–6.9% = 9.9% of the photons), will be reflected off the perovskite/air, and then escape out of the perovskite/glass interface. Therefore, accounting for the small attenuation due to self-absorption, the total escape probability for the perovskite NC films is estimated to be

Following Richter *et. al*'s equation 3,[51] the relation between internal PLQY (), and measured PLQY () is given by

Substituting the measured external PLQY of 70%, ( ) and total escape probability of 32.4%, (), we obtain internal PLQY () = 0.878 or 87.8%. We note that this expression accounts for the photon recycling and illustrates that the external measured PLQY can deviate considerably from the internal PLQY.

ICP-MS Analysis

To support the existence of this "stripped" Pb-ligand (EDTA, GL) complex in the sediment, we have performed an ICP-MS analysis of the resulting precipitates (which includes the potential Pb-ligand complex and undissolved ligand) after repeated washing with toluene (10 times). As both EDTA and GL have very low solubility in toluene, this process effectively disperses and removes the remaining NCs while retaining the Pb-ligand complexes in the residue. To rule out the spurious lead content arising from remaining NCs, toluene supernatant from the final washing step was also subjected to ICP analysis. The result clearly shows an increasing quantity of precipitate lead content in the order of GL (518 µg mg^{-1})>EG (428 µg mg^{-1})>EDTA (354 µg mg^{-1})-treated samples when compared to the final supernatant (nearly 0 ug mg^{-1}). To estimate whether EDTA and GL have different Pb^{2+} complexation ability, we calculated the binding energy between the two ligands and a Pb^{2+} ion, see **Extended Data Figure 10**. The complexes show a hemidirected coordination of the ligands, with EDTA endowed with a significantly higher binding energy to Pb^{2+} than GL, by 0.80 eV.

Fabrication of $MAPb(I_{1-x}Br_x)_3$ NC LEDs

Our final device stack, for which a schematic and a SEM cross-sectional image is shown in **Fig. 3a and b**, includes a "triple-layer" hole-injection layer, comprising Poly(3,4-ethylenedioxythiophene):poly(*p*-styrene sulfonate) (PEDOT:PSS), Poly[N,N'–

bis(4-butylphenyl)-N,N'-bisphenylbenzidine] (poly-TPD) and the deep work-function polymer - poly[(9,9-dioctylfluorenyl-2,7-diyl)-co-(4,4'-(N- (4-sec-butylphenyl)diphenylamine)] (TFB), followed by a thin dense layer of the perovskite NCs (~ 30nm), capped with the electron transport layer of 2,2',2''-(1,3,5-Benzinetriyl)-tris(1-phenyl-1-Hbenzimidazole) (TBPi) and a lithium fluoride/aluminium cathode. Typically, Indium tin oxide (ITO)-coated glass substrates were cleaned by an ultra-sonification process in deionised water, acetone, and isopropanol for 10 min. PEDOT:PSS was spin-coated onto an ITO substrate at 5,000 rpm for 40 s. The coated substrates were transferred to an N_2-filled glove box and annealed at 140 °C for 10 min. Poly-TPD solution (15 mg ml^{-1}) in chlorobenzene and TFB solution (20 mg mL^{-1}) in p-xylene was sequentially spin-coated onto the substrates at 4,000 rpm for 40 s. Each layer was annealed at 140 °C for 30 min. The $MAPbI_2Br$ NCs were spin-coated onto the substrates at 2,000 rpm for 40 s. 70 nm thick layer of TPBi, 1 nm thick layer of LiF, and 80 nm thick layer of Al were sequentially deposited using a thermal evaporation system.

Solid-state 13C NMR

Solid-state ^{13}C MAS NMR was performed at 9.4 T (KBSI Western Seoul Center) using a 4 mm Bruker triple resonance probe. The prepared nanocrystals were packed into reduced volume zirconia rotors under nitrogen atmosphere and were spun at 8 kHz. ^{13}C data were acquired by ^{1}H-^{13}C Hartmann-Hahn cross polarization sequence with 100 kHz SPINAL64 ^{1}H decoupling.

Solution HNMR

In order to assess the interaction between the ligands and Pb^{2+}, we measured ^{1}H NMR spectra of the ligands mixed with PbI_2. In **Fig. 4b**, we have annotated structural

diagrams of the ligands, indicating the different moieties responsible for the NMR resonances and the different binding units present in GL, namely, glutamine (glu), cysteine (cys) and glycine (gly). In **Fig. 4c** and **Extended Data Fig. 9,** we observe that both ^{1}H signals from EDTA shift downfield and broaden, indicating multidentate complexation of EDTA to Pb^{2+}. We mixed GL and PbI_2 in *d*-DMSO and observed two changes: (i) significant broadening and increased chemical shifts of the cysteinyl β_{cys} resonance and (ii) decreased chemical shifts of the amide NH_{cys} resonances. The first change indicates that Pb^{2+} binds to cysteinyl sulphur[54,55]. The shift of amide NH_{cys} resonances is likely caused by the coordination of the amide NH to the S-bound Pb^{2+}, as demonstrated for the case of chemically similar Cd^{2+} binding to GL[56]. We also observe a weakening of the geminal ^{2}J coupling of glutamine's beta protons (β_{glu}), indicating that the COOH is also bound to Pb^{2+}. The glycine's alpha proton (α_{gly}) displayed no observable shift upon addition of PbI_2, in agreement with previous work showing that the COO^- group of glycine does not bind to Pb^{2+} [57]. In **Extended Data Fig. 9** we show the ^{1}H NMR spectra when both ligands (E+G) are mixed with PbI_2. We observe that all of the interaction changes present in the solutions containing the individual ligands are also present with the combined ligands, indicating that when both ligands are combined in the E+G mixture, they maintain their individual interactions with PbI_2. We show the proposed molecular interactions of the E+G ligands with Pb^{2+} on the NC surface in **Fig. 4d**. We conclude that both EDTA and GL can coordinate with Pb^{2+} via the aforementioned binding groups in this system.

DFT approach:

We model the interaction of glutathione (GL) and EDTA on perovskite surfaces by the state-of-the-art DFT calculations, including dispersion interactions, to mimic the surface chemistry of

perovskite NCs. Due to the uncertain nature of surfaces and their terminations in mixed halide perovskites, we focus here on $MAPbI_3$, for which we have a trustful surface picture. We will evaluate in due course the possible impact on the results of considering a single halide in place of a mixed halide. All our results are obtained considering a PbI_2-terminated surface, which is representative of the extreme situation of a fully unpassivated perovskite surface exposing undercoordinated surface Pb atoms.

We proceed based on the following reasoning:

1) halide demixing is triggered by defect formation and/or migration.

2) most defects and migration channels are on surfaces, so surface passivation blocks defect formation, ion migration, and demixing.

3) surface passivation molecules should bind effectively to the perovskite surface and pack tightly, thus being an effective migration blocker.

4) We consider the adsorption of single GL and EDTA molecules and then move to GL-GL, EDTA-EDTA, and GL-EDTA coadsorption.

Since GL is quite a complex molecule, we initially model what chemical fragment within GL is most strongly interacting with the perovskite surface.

Thus, we decomposed GL and EDTA into the possible binding moieties and calculated the fragments binding energy (BE) to the perovskite, see **Extended Data Fig.10**. The binding energy is defined as: **BE=E(mol@surface) – E(mol) – E(surface)** **(1)**

The results show that the ammidic fragment of GL is the most strongly binding one; see **Extended Data Fig. 10**. Typically, the calculated BE of GL is very high (-1.85 eV), coming from a partial sum of all binding ingredients. EDTA interaction with the perovskite shows a lower BE

than GL (-1.60 vs. -1.85 eV), with EDTA mainly binding through carboxylic groups. Although the tertiary amminic groups may show a higher BE to Pb than COOH (**Extended Data Fig. 10**), steric hindrance prevents EDTA from exploiting such interaction.

To evaluate the energetics of forming a compact monolayer on the perovskite surface, thus effectively blocking all possible undercoordinated Pb atoms acting as defect-nucleating centres we next evaluated the BE of two interacting GL, two interacting EDTA, and an interacting GL/EDTA pair on the perovskite surface. In the case of two or more interacting molecules, the BE includes both surface-molecule and molecule-molecule interactions. The E+G pair was found to have the highest binding energy, enhanced by a synergistic effect between GL and EDTA. Intermolecular hydrogen bonding between carboxylic groups of the GL and EDTA provides extra stabilisation to these surface adsorbed molecules, leading to a BE of -4.45 eV (**Extended Data Fig. 10**).

Most notably, while both GL and EDTA may form a compact monolayer on the perovskite surface, *the strongest interaction comes from the synergistic binding of GL and EDTA*, for which the highest BE to the perovskite surface is calculated. Notice that in the case of two (or more) interacting molecules, the BE includes surface/molecule and molecule/molecule interactions, delivering s total BE higher than the sum of the two individual BEs. In the E+G case, the intermolecular contribution, related to intermolecular hydrogen bonding between carboxylic groups, provides an extra stabilisation to the surface adsorbed molecules, delivering the highest BE (-4.45 eV), higher than the GL/GL and EDTA/EDTA BEs; see **Extended Data Fig. 10**.

To connect the calculated BEs to the defect-blocking properties of the respective surface-adsorbed molecules, we have considered the energetics for formation of iodine Frenkel defect

pair (*i.e.* iodine vacancy / interstitial iodine) at the surface. These defects are the energetically most probable defects at the PbI_2-terminated perovskite surface; thus, they constitute a case study to evaluate the impact of surface adsorbed molecules on defect formation energies. We thus calculated the formation energy of an iodine Frenkel defect pair at the PbI_2-terminated perovskite surface without passivating molecules and in the presence of GL and of E+G.

Formation of an iodine Frenkel defect on the PbI_2-terminated perovskite surface has very low formation energy (0.03 eV), in line with the instability of the unpassivated surface (complete surface passivation by MAI raises the formation energy to 0.84 eV). GL surface passivation raises the formation energy to 0.15 eV, with E+G further raising it to 0.18 eV. This clearly demonstrates the GL surface defect blocking effect and the synergistic E+G effect. To put this value into context, when modelling the PEO interaction with the same perovskite surface, we calculated a defect formation energy increase of 0.08 eV for a complete monolayer of (CH_3OCH_3, mimicking PEO) thus, the values obtained here for GL and E+G are to be considered extremely high.

To sum up, we have evaluated the binding of GL, EDTA, and E+G on the perovskite surface and evaluated their ability as Frenkel defect blocking agents. The results show a synergistic effect of GL+EDTA in delivering the highest surface binding energy and the highest defect blocking activity. The key to efficient surface passivation is the concurrent action of strong molecule/surface and molecule/molecule interactions.

All simulations have been carried out with the Quantum Espresso program package[57]. DFT calculations have been carried out on the (001) $MAPbI_3$ surface within the supercell approach by using the Perdew-Burke-Ernzerhof (PBE)[58] functional by using ultrasoft pseudopotentials (shells explicitly included in calculations: I 5s, 5p; N, C 2s, 2p; O 2s 2p; H 1s; Pb 6s, 6p,

5d; S 3s 3p) and a cutoff on the wavefunctions of 25 Ryd (200 Ryd on the charge density). DFT-D3 dispersion interactions were included in the calculation[58].

Slabs models have been built starting from the tetragonal phase of $MAPbI_3$[59] by fixing cell parameters to the experimental values and generating a 2x2 supercell in a and b directions. A 10 Å of vacuum was added along the non-periodic direction perpendicular to the slabs in all cases. A symmetric disposition of the organic cations on the external layers of the slabs has been adopted in all cases, leading to supercells with zero average dipole moments. Such an arrangement of organic cations provided a flat electrostatic potential in the vacuum region of the supercells for all the modelled slabs.

Methods extended reference list:

50 Zhao, B. *et al.* High-efficiency perovskite–polymer bulk heterostructure light-emitting diodes. *Nature Photonics* **12**, 783-789, doi:10.1038/s41566-018-0283-4 (2018).

51 Richter, J. M. *et al.* Enhancing photoluminescence yields in lead halide perovskites by photon recycling and light outcoupling. *Nature Communications* **7**, 13941, doi:10.1038/ncomms13941 (2016).

52 Cho, C. *et al.* The role of photon recycling in perovskite light-emitting diodes. *Nature Communications* **11**, 611, doi:10.1038/s41467-020-14401-1 (2020).

53 Salehi, A., Chen, Y., Fu, X., Peng, C. & So, F. Manipulating Refractive Index in Organic Light-Emitting Diodes. *ACS Applied Materials & Interfaces* **10**, 9595-9601, doi:10.1021/acsami.7b18514 (2018).

54 Sisombath, N. S. & Jalilehvand, F. Similarities between N-Acetylcysteine and Glutathione in Binding to Lead(II) Ions. *Chemical Research in Toxicology* **28**, 2313-2324, doi:10.1021/acs.chemrestox.5b00323 (2015).

55 Mah, V. & Jalilehvand, F. Lead(II) Complex Formation with Glutathione. *Inorganic Chemistry* **51**, 6285-6298, doi:10.1021/ic300496t (2012).

56 Delalande, O. *et al.* Cadmium–glutathione solution structures provide new insights into heavy metal detoxification. *The FEBS Journal* **277**, 5086-5096, doi:10.1111/j.1742-4658.2010.07913.x (2010).

57 Giannozzi, P. *et al.* QUANTUM ESPRESSO: a modular and open-source software project for quantum simulations of materials. *Journal of Physics: Condensed Matter* **21**, 395502, doi:10.1088/0953-8984/21/39/395502 (2009).

58 Perdew, J. P., Burke, K. & Ernzerhof, M. Generalized Gradient Approximation Made Simple. *Physical Review Letters* **77**, 3865-3868, doi:10.1103/PhysRevLett.77.3865 (1996).

59 Poglitsch, A. & Weber, D. Dynamic disorder in methylammoniumtrihalogenoplumbates (II) observed by millimeter-wave spectroscopy. *The Journal of Chemical Physics* **87**, 6373-6378, doi:10.1063/1.453467 (1987).

FIGURE LEGENDS:

Figure 1. Illustration of NC synthesis. a, Synthesis and ligand treatment steps: (i) Dissolution of perovskite precursors in acetonitrile (ACN) and methylamine (MA), (ii) NC synthesis by modified LARP, and (iii) post-synthetic ligand treatment. **b**, chemical structures of ligands used.

Fig. 2. Impact of ligand treatment on the solution photoluminescence and NC structural properties. a, Absorption and PL spectra of as-synthesised $MAPb(I_{1-x}Br_x)_3$ NCs in solution. **b,** PL spectra of NC films following post-synthetic treatment with GL, EDTA, and EDTA + GL (E+G). **c,** Excitation fluence dependence of PLQE of NC thin films before and after ligand treatment, measured in an integrating sphere. **d,e**, High-resolution transmission electron micrograph (HR-TEM) image for NCs before and after ligand treatment with E+G, respectively. **f,** XRD for the NCs films before and after ligand treatment. **g,h**, Decay associated difference spectra from a global fit of TAS measurements of neat- and E+G-capped NCs, respectively. Solid and dashed lines are spectra before and after 30 s of exposure to a 7.1 W cm^{-2} 405 nm CW laser. Blue, green, and red traces correspond to decay components with time constants of ~400 fs, ~14 ps, and ~280 ps, respectively. Red arrows indicate the red edge of the spectra, where changes in the bandgap of the material would result in changes to the bleaching of the sample due to band filling.

Figure 3. Device characterisation of mixed halide $MAPb(I_{1-x}Br_x)_3$ NC-LEDs: a, Schematic illustration of $MAPb(I_{1-x}Br_x)_3$ NC-LED architecture and scanning electron microscopy (SEM) image showing the cross section of a device; thickness of each layer is confirmed by SEM image: PEDOT:PSS/Poly-TPD/TFB HTLs (30 nm), NC emission layer (20 nm), TPBi ETL (70 nm), LiF/Al electrode (80 nm). **b,** Energy band diagram of the materials employed in these LEDs, from references[44-46]. Operational characteristics for LEDs incorporating neat and E+G ligand treated NC layers; **c,** Current density–voltage and luminance(L)-voltage curves, **d,** EQE-current density curves, **e,** device performance parameters of best-performing LEDs (LE is luminous efficiency)**. f,** EL spectra at different time intervals for LEDs held at a constant current density of 1.5 mA cm^{-2} **g,** EL spectra at different current densities (mA cm^{-2}).

Figure 4. Characterisation of ligand-NC surface interactions using NMR spectroscopy: a, Molecular structure of EDTA and GL. Peaks a and b are characteristic of CH_2 as labelled in the molecular structure of EDTA while peaks α, β, and γ are characteristic of CH_2 in GL. **b**, ^{13}C solid-state NMR spectra of neat and ligand (GL, EDTA, E+G) treated NCs. Insets show ligand structure. **c,** Solution ^{1}H NMR spectra of E+G with and without PbI_2 in d-DMSO solutions. **d,** Proposed molecular interactions of GL and EDTA with Pb^{2+} atoms on the NC surface.

Figure 5. Optimised structures of two interacting surface adsorbed **a,** GL, **b,** EDTA, and **c,** one GL and one EDTA molecule, along with calculated total biding energies (E_b) and their intermolecular contribution (ΔE_{inter}) in eV calculated with respect to the isolated surface adsorbed molecules

(E_b=1.85 and 1.60 eV for GL and EDTA, respectively). **d,** Optimised structure of an iodine Frenkel defect pair – defective sites highlighted by red and blue circles - in the presence of adsorbed GL+EDTA along with the increase of defect formation energy compared to the unpassivated surface ($\Delta E_{Frenkel}$, in eV).

Extended Data Figure 1. Extended Data Figure 1. Characteristics of NCs with and without ligand treatment.: Photothermal deflection spectroscopy (PDS) spectra of perovskite neat NCs vs. NCs-treated with EDTA+GL films deposited on quartz substrates. The inset shows the calculation of the average Urback energy for these two samples. Time-resolved PL decay of neat NCs and NCs treated with EDTA+GL **b**, solution dispersed in toluene, and **c**, films. **d,** time-resolved photoluminescence corresponding lifetimes of the neat NCs, and E+G-treated NCs. **e,** FTIR for $MAPb(I_xBr_{1-x})_3$ perovskite NCs: drop-casted films from NCs synthesised in oleic acid and after the treatment with EDTA, GL, or E+G ligands. **f**, XPS results for NCs before and after ligand treatment, which shows the ligand-treated NC final product approximately corresponds to $MAPb(I_{0.4}Br_{0.6})_3$, whereas the original perovskite NC was synthesized using the composition of $MAPb(I_{0.67}Br_{0.33})_3$.

Extended Data Figure 2. High-resolution transmission electron micrograph (HR-TEM) images for NCs.: a-b,HR-TEM image for neat NCs. **c,** fast Fourier transformation (FFT) of the selected region in panel (b), where interplanar lattice spacing of cubic phase is spaced by 0.6 and 0.42 nm for the {001}, and {110} family of planes. **d-e,** HR-TEM image for neat NCs after ligand treatment with E+G ligands. **f,** FFT of the selected region in panel (e) showing a similar cubic structure as neat NCs.

Extended Data Figure 3. **Impact of ligands upon the photoluminescence and nanocrystal structural properties.** **a**, Schematic of TAS procedure. Coloured circles represent PL measurements before (black) and after (red) illumination with a 405 nm laser. Duration of periodic re-exposure, T (10 s for neat, 3 s for E+G-treated NCs), maintained a stable PL wavelength during TAS scans. For neat NCs, PL wavelength was initially 649 nm, 669±1 nm after exposure. PL of E+G-treated NCs was initially 628 nm, 632±1 nm after exposure. TAS of neat/E+G-treated NCs before (**b**/**d**) and after (**c**/**e**) illumination. Transients of neat/E+G-treated NCs before (**f,g/j,k**) and after (**h,i/l,m**) illumination. Traces are average signal in wavelength ranges chosen to highlight wavelength-dependent dynamics. Blue, green, yellow, red traces for the neat NCs/E+G-treated NCs correspond to 560-600/550-580 nm, 600-640/580-610 nm, 640-680/610-640 nm, 680-720/640-670 nm. Black dashed lines are global fit to a tri-exponential function. **n**, Time constants before (after) illumination of each NC sample, found by a global fit of TA spectra. Colours refer to those in Figure 2 (**g**, **h)**.

Extended Data Figure 4. Halide segregation in diluted neat NCs. Normalized photoluminescence spectra of spin-cast films of neat NCs and polymethyl methacrylate (PMMA), in a NC:PMMA mass ratio of **a,** 1.03 and **b,** 0.006. A 405 nm CW laser was used as an excitation source and caused halide segregation, with the duration of irradiation indicated in the legend. The redshifted shoulder developed during irradiation is ascribed to the recombination from within an iodide-enriched minority phase with a smaller bandgap. The redshifted shoulder showed no dependence on the NC concentration in the film, indicating that segregation can occur in isolated NCs. **c,**

Confocal PL images and **d,** normalized PL spectrum of spin-cast films of neat NCs over time under constant excitation with 405 nm CW laser. PL spectrum was obtained from selected region of panel (c). **e,** Confocal PL images and **f,** normalized PL spectrum of spin-cast films of neat NCs and PMMA, in a NC:PMMA mass ratio of 0.001 over time under constant excitation with 405 nm diode laser. PL spectrum was obtained from selected region of panel (e).

Extended Data Figure 5. EL spectra stability in the mixed halides $MAPb(I_xBr_{1-x})_3$ NC-LEDs with different ligand treatment.: a, Current density–voltage (J–V) curves **b**, luminous (L) versus voltage (V–L) curves **c**, EL-EQE curves of NC-LEDs current density (J–EQE) **d-f**, EL spectra of NC-LEDs at different bias voltage. **g-l**, EL spectra of NC-LEDs with different ligand treatment at a constant current density of 10 mA cm^{-2} **j-l,** EL spectra of the second ligand treated NC-LEDs with 1- adamantane carboxylic acid (ADAC) at a constant current density of 10 mA cm^{-2}.

Extended Data Figure 6. Characteristics of NCs films with the different charge-transporting layers (CTLs).: a, Time-resolved photoluminescence decays of E+G-treated NCs films with various CTLs (excitation at 450 nm), (PNCs: perovskite NCs, PD: PEDOT:PSS, P-TPD: Poly-TPD). **b**, photoluminescence intensities of E+G-treated NCs films with various CTLs (excitation at 350 nm). PL decays significantly faster, and PL intensity is reduced in the presence of a poly-TPD hole transporting layer (HTL), while little change is observed with a TPBi electron transporting layer (ETL). This result shows that exciton quenching significantly affects the interface between poly-TPD and the NCs, resulting in a deterioration of device efficiency. **c,** Time-resolved photoluminescence decays of E+G-treated NCs films with various HTLs (excitation at 450 nm). **d**, photoluminescence intensities of E+G-treated NCs films with various HTLs (excitation at 450 nm). TFB HTLs show longer PL decays and larger PL intensity compared to the Poly-TPD HTLs, indicating less exciton quenching at the interface between NCs and TFB HTLs. **e,** Photoemission cut off energy, and **f,** the valence-band region of neat and E+G-treated NCs from ultraviolet photoemission spectroscopy (UPS) spectra. **g–h**, Optical band gap of Neat NCs, and E+G-treated NCs.

Extended Data Figure 7. Device characteristics and EL spectra stability in the mixed halides $MAPb(I_xBr_{1-x})_3$ NC-LEDs.: a, Schematic illustrations of the NC-LED configuration showing the device architecture: ITO/PEDOT:PSS/poly-TPD/$MAPb(I_{1-x}Br_x)_3$ NCs/TPBi/LiF/Al. **b**, Current density–voltage (J–V) curves, and luminous (L) versus voltage (V–L) of NC-LEDs. **c**, luminous efficiency (LE) versus current density (J–LE) curves of NC-LEDs. **d**, EL-EQE curves of NC-LEDs current density (J–EQE). **e-f**, EL spectra of OA-LEDs, E+G-treated NC-LEDs at different bias voltage. **g**, EL peak of OA-LEDs, E+G-treated NC-LEDs at different current density. **h-i**, EL peak of OA-LEDs, E+G-treated NC-LEDs at a constant current of 0.5 mA cm^{-2} for one hour, and EL peak of same device rest in the glove box for different times. Shifted EL peak position under the constant current density of 0.5 mA cm^{-2} recovers to the initial peak position after rest in the glove box for 6 hours, indicating the reversibility of halide segregation.

Extended Data Figure 8: Peak EQE histogram and operation stability of mixed halides $MAPb(I_xBr_{1-x})_3$ NC-LEDs. a, The peak EQE histogram E+G-treated NC-LEDs was collected

from 25 devices. **b,** Operational stability of E+G-treated NC-LEDs measured in air at a constant current of 0.1 (L_0 = 30 cd m^{-2}, EQE_0 = 16.4%), 1 (L_0 = 150 cd m^{-2}, EQE_0 = 9.1%), and 10 mA cm^{-2} (L_0 = 600 cd m^{-2}, EQE_0 = 3.3%). EL spectra of NCs-LEDs with neat **c,d**, and E+G ligand treated **h,I**, NC layers at a different lifetime of T_x with a constant current density of 1 mA cm^{-2} and 10 mA cm^{-2}.

Extended Data Figure 9. ^{1}H NMR spectra of solutions: a, $MAPb(I_xBr_{1-x})_3$ NCs before and after an treatment with E+G mixture in d-toluene. **b,** Magnification selected region of the 1H-NMR spectra between 5.4 and 5.6 ppm in panel a, showing details of the proton bound to C=C of OA/OLA in; reveals fine structure on top of the broad resonance after ligand treatment, which is an indication of (OA/OLA) free ligands. **c,** systematic addition of E+G to PbI_2 in d-DMSO solutions. **d–e**, EDTA, GL and E+G ligands in d-DMSO, and D2O, respectively, where when both ligands are combined in the E+G mixture, they maintain their individual peaks' positions, indicating there is no chemical interaction between the two ligands. **f,** GL in d-DMSO versus in d-DMSO mixture with D_2O showing the disappearing of amide NH, exchangeable protons, peaks in the presence of D_2O. **g–h**, systematic addition of EDTA, and GL to PbI_2 in d-DMSO solutions, respectively.

Extended Data Figure 10. **DFT-optimised structures of surface adsorbed ligands: a,** Structure of GL (left) and EDTA (right) along with fragments used to study its interaction with the perovskite. DFT-optimised structures of surface absorbed **b,** GL, **c,** EDTA, **d,** one GL, and one EDTA molecule, **e,** two EDTA molecules, **f,** and two GL molecules. The optimised structure of an iodine Frenkel defect pair – defective iodine atoms in yellow – **g,** on the bare PbI_2-terminated perovskite surface, **h,** in the presence of adsorbed GL and, **i,** in the presence of adsorbed GL+EDTA. The iodine vacancy is highlighted with the dashed circle. **j,** Binding energies of fragments and complete molecules to the PbI2-terminated perovskite surface. Data in parenthesis shows the data per adsorbed molecule. **k,** DFT-optimised structures of the $[Pb(EDTA/GL)]^{2+}$ complexes and the relative binding energy showing stronger binding of EDTA to Pb^{2+} than GL by 0.80 eV.

Online content

Any methods, additional references, Nature Research reporting summaries, source data, statements of data availability and associated accession codes are available at (link).

Acknowledgements

This work was partially funded by the Engineering and Physical Sciences Research Council (EPSRC) U.K. through Grants EP/M005143/1 and EP/M015254/2. This work is part of the

PEROCUBE project, which has received funding from the European Union's Horizon 2020 research and innovation program under grant agreement No. 861985. A.S., H.S., Y.H., R.S. and R.H.F. acknowledge funding and support from the SUNRISE project (EP/P032591/1), EPSRC. A.S. and R.H.F. acknowledge support from UKIERI project. A.S. acknowledges funding and support from DST, IISc and MHRD. R.S. acknowledge The Royal Society - Newton International Fellowship. M.L.C. acknowledges financial support from Achievement Rewards for College Scientists (ARCS) Foundation, Oregon Chapter. This study was partially supported by the National Research Foundation of the Republic of Korea (NRF-2018R1C1B6005778, 2018R1A2B2006198, 2020R1A4A1018163, and 2019R1A6A1A10073437) and the Materials Innovation Project (NRF-2020M3H4A3081793) funded by National Research Foundation of Korea. NMR data were acquired on 400MHz Solid state NMR spectrometer (AVANCE III HD, Bruker, Germany) at KBSI Western Seoul Center. The experiments of HR-TEM, XPS, NMR, confocal PL and SEM were supported by UNIST Central Research Facilities (UCRF). Y.H. would like to thank Dr Dr. Mohsen Danie for assistance with TEM, Safwat M. Rabea, Dr Tarek S. Ibrahim, Dr Ahmed M. Ali and Dr Trevor Janes for assistance with NMR analysis, and to Dr. Mohammed Nour Ahmed for his advice on Figure 1. Y.H. acknowledges funding and support from LXT AI (Canada).

Author contributions

Y.H. initiated the project, synthesised the NCs, conceived the multidentate ligand approach developed and performed the ligand treatment process and performed with J.H.P. the TEM, UV–vis absorption, photoluminescence, and XRD measurement. Y.H. and H.J.S. planned the experiments and overall project targets. Y.H. coordinated

collaboration efforts. J.H.P. fabricated LED devices. A.S. assisted in the NCs synthesis and performed the PLQY and Photothermal deflection spectroscopy (PDS) measurements. R.S. assisted with the PLQY and PDS measurements. Y.H, M.L.C. M.J., C.Y., and J.L. performed the NMR experiments and analysed its data. J.H.P. measured the STEM and Y.H. performed their analysis. J.H.P. and B.R.L. assisted with the materials and LED characterisation process. M.H.S., H.C., S.H.P., and B.R.L. supported the material, and device characterisations. J.H.P., and B.R.L. carried out the device stability tests. M.L.C. and J.C.S. designed and executed the TA experiments and M.L.C. performed data analysis. E.M., E.R., and F.D.A conducted the computational simulations. C.Y.W., B.R.L., R.H.F., and H.J.S. supervised the work undertaken in their laboratories, which has contributed to this manuscript. Y.H. drafted the first version of the manuscript, with assistance from J.C.S., C.Y.W., and H.J.S.. All the authors have read and commented upon or contributed to the writing of the manuscript. Y.H. and J.H.P. contributed equally to this work.

Competing interests: The authors declare the following competing financial interest: HJS is a co-founder of Oxford PV ltd, which is commercialising perovskite-based photovoltaics. HJS and RHF are co-founders of Helio Display Materials Ltd, which is commercialising perovskite materials for light-emitting applications.

Additional Information (Extended Data information is available for this paper at (link)

Reprints and permissions information is available at www.nature.com/reprints.

Correspondence and requests for materials should be addressed to Y.H. or H.J.S.

Yasser Hassan: Yasser.hassan@physics.ox.ac.uk; yasserhassan8085@gmail.com

Cathy Wong: cwong3@uoregon.edu

Bo Ram Lee: brlee@pknu.ac.kr

Henry Snaith: henry.snaith@physics.ox.ac.uk

References

1 Tan, Z.-K. *et al.* Bright light-emitting diodes based on organometal halide perovskite. *Nat Nano* **9**, 687-692, doi:10.1038/nnano.2014.149 http://www.nature.com/nnano/journal/v9/n9/abs/nnano.2014.149.html#supplementary-information (2014).

2 Xiao, Z. *et al.* Efficient perovskite light-emitting diodes featuring nanometre-sized crystallites. *Nature Photonics* **11**, 108 (2017).

3 Zhao, X. & Tan, Z.-K. Large-area near-infrared perovskite light-emitting diodes. *Nature Photonics* **14**, 215-218, doi:10.1038/s41566-019-0559-3 (2020).

4 Zhao, B. *et al.* High-efficiency perovskite–polymer bulk heterostructure light-emitting diodes. *Nature Photonics* **12**, 783-789, doi:10.1038/s41566-018-0283-4 (2018).

5 Hassan, Y. *et al.* Facile Synthesis of Stable and Highly Luminescent Methylammonium Lead Halide Nanocrystals for Efficient Light Emitting Devices. *Journal of the American Chemical Society* **141**, 1269-1279, doi:10.1021/jacs.8b09706 (2019).

6 Protesescu, L. *et al.* Nanocrystals of Cesium Lead Halide Perovskites (CsPbX3, X = Cl, Br, and I): Novel Optoelectronic Materials Showing Bright Emission with Wide Color Gamut. *Nano Letters* **15**, 3692-3696, doi:10.1021/nl5048779 (2015).

7 Tian, Y. *et al.* Highly Efficient Spectrally Stable Red Perovskite Light-Emitting Diodes. *Advanced Materials* **30**, 1707093, doi:doi:10.1002/adma.201707093 (2018).

8 Chang, J. *et al.* Enhanced Performance of Red Perovskite Light-Emitting Diodes through the Dimensional Tailoring of Perovskite Multiple Quantum Wells. *The Journal of Physical Chemistry Letters* **9**, 881-886, doi:10.1021/acs.jpclett.7b03417 (2018).

9 Cao, Y. *et al.* Perovskite light-emitting diodes based on spontaneously formed submicrometre-scale structures. *Nature* **562**, 249-253, doi:10.1038/s41586-018-0576-2 (2018).

10 Burlakov, V. M., Hassan, Y., Danaie, M., Snaith, H. J. & Goriely, A. Competitive Nucleation Mechanism for CsPbBr3 Perovskite Nanoplatelet Growth. *The Journal of Physical Chemistry Letters* **11**, 6535-6543, doi:10.1021/acs.jpclett.0c01794 (2020).

11 Wang, Z. *et al.* Efficient ambient-air-stable solar cells with 2D–3D heterostructured butylammonium-caesium-formamidinium lead halide perovskites. *Nature Energy* **2**, 17135, doi:10.1038/nenergy.2017.135 https://www.nature.com/articles/nenergy2017135#supplementary-information (2017).
12 Zhou, Y. *et al.* Benzylamine-Treated Wide-Bandgap Perovskite with High Thermal-Photostability and Photovoltaic Performance. **7**, 1701048, doi:doi:10.1002/aenm.201701048 (2017).
13 Yan, J., Qiu, W., Wu, G., Heremans, P. & Chen, H. Recent progress in 2D/quasi-2D layered metal halide perovskites for solar cells. *Journal of Materials Chemistry A* **6**, 11063-11077, doi:10.1039/C8TA02288G (2018).
14 Lee, D. S. *et al.* Passivation of Grain Boundaries by Phenethylammonium in Formamidinium-Methylammonium Lead Halide Perovskite Solar Cells. *ACS Energy Letters* **3**, 647-654, doi:10.1021/acsenergylett.8b00121 (2018).
15 Zhang, X. *et al.* Bright Perovskite Nanocrystal Films for Efficient Light-Emitting Devices. *The Journal of Physical Chemistry Letters* **7**, 4602-4610, doi:10.1021/acs.jpclett.6b02073 (2016).
16 Chiba, T. *et al.* Anion-exchange red perovskite quantum dots with ammonium iodine salts for highly efficient light-emitting devices. *Nature Photonics* **12**, 681-687, doi:10.1038/s41566-018-0260-y (2018).
17 Xiao, Z. *et al.* Mixed-Halide Perovskites with Stabilized Bandgaps. *Nano Letters* **17**, 6863-6869, doi:10.1021/acs.nanolett.7b03179 (2017).
18 Barker, A. J. *et al.* Defect-Assisted Photoinduced Halide Segregation in Mixed-Halide Perovskite Thin Films. *ACS Energy Letters* **2**, 1416-1424, doi:10.1021/acsenergylett.7b00282 (2017).
19 Meggiolaro, D., Mosconi, E. & De Angelis, F. Formation of Surface Defects Dominates Ion Migration in Lead-Halide Perovskites. *ACS Energy Letters* **4**, 779-785, doi:10.1021/acsenergylett.9b00247 (2019).
20 Vashishtha, P. & Halpert, J. E. Field-Driven Ion Migration and Color Instability in Red-Emitting Mixed Halide Perovskite Nanocrystal Light-Emitting Diodes. *Chemistry of Materials* **29**, 5965-5973, doi:10.1021/acs.chemmater.7b01609 (2017).
21 Yang, Z. *et al.* Stabilised Wide Bandgap Perovskite Solar Cells by Tin Substitution. *Nano Letters* **16**, 7739-7747, doi:10.1021/acs.nanolett.6b03857 (2016).
22 Bush, K. A. *et al.* Compositional Engineering for Efficient Wide Band Gap Perovskites with Improved Stability to Photoinduced Phase Segregation. *ACS Energy Letters* **3**, 428-435, doi:10.1021/acsenergylett.7b01255 (2018).
23 Yi, C. *et al.* Entropic stabilisation of mixed A-cation ABX3 metal halide perovskites for high performance perovskite solar cells. *Energy & Environmental Science* **9**, 656-662, doi:10.1039/C5EE03255E (2016).
24 Hu, M., Bi, C., Yuan, Y., Bai, Y. & Huang, J. Stabilized Wide Bandgap MAPbBrxI3–x Perovskite by Enhanced Grain Size and Improved Crystallinity. **3**, 1500301, doi:doi:10.1002/advs.201500301 (2016).
25 Gualdrón-Reyes, A. F. *et al.* Controlling the Phase Segregation in Mixed Halide Perovskites through Nanocrystal Size. *ACS Energy Letters* **4**, 54-62, doi:10.1021/acsenergylett.8b02207 (2019).

26 Zhou, Y. *et al.* Composition-Tuned Wide Bandgap Perovskites: From Grain Engineering to Stability and Performance Improvement. **28**, 1803130, doi:doi:10.1002/adfm.201803130 (2018).
27 Abdi-Jalebi, M. *et al.* Maximising and stabilising luminescence from halide perovskites with potassium passivation. *Nature* **555**, 497, doi:10.1038/nature25989 (2018).
28 Belisle, R. A. *et al.* Impact of Surfaces on Photoinduced Halide Segregation in Mixed-Halide Perovskites. *ACS Energy Letters* **3**, 2694-2700, doi:10.1021/acsenergylett.8b01562 (2018).
29 Zhang, L. & Sit, P. H. L. Ab initio study of the dynamics of electron trapping and detrapping processes in the CH3NH3PbI3 perovskite. *Journal of Materials Chemistry A* **7**, 2135-2147, doi:10.1039/C8TA09512D (2019).
30 Li, W., Liu, J., Bai, F.-Q., Zhang, H.-X. & Prezhdo, O. V. Hole Trapping by Iodine Interstitial Defects Decreases Free Carrier Losses in Perovskite Solar Cells: A Time-Domain Ab Initio Study. *ACS Energy Letters* **2**, 1270-1278, doi:10.1021/acsenergylett.7b00183 (2017).
31 Meggiolaro, D. *et al.* Iodine chemistry determines the defect tolerance of lead-halide perovskites. *Energy & Environmental Science* **11**, 702-713, doi:10.1039/C8EE00124C (2018).
32 Motti, S. G. *et al.* Controlling competing photochemical reactions stabilises perovskite solar cells. *Nature Photonics* **13**, 532-539, doi:10.1038/s41566-019-0435-1 (2019).
33 Shao, Y. *et al.* Grain boundary dominated ion migration in polycrystalline organic–inorganic halide perovskite films. *Energy & Environmental Science* **9**, 1752-1759, doi:10.1039/C6EE00413J (2016).
34 Bischak, C. G. *et al.* Origin of Reversible Photoinduced Phase Separation in Hybrid Perovskites. *Nano Letters* **17**, 1028-1033, doi:10.1021/acs.nanolett.6b04453 (2017).
35 Wu, T. *et al.* High-Performance Perovskite Light-Emitting Diode with Enhanced Operational Stability Using Lithium Halide Passivation. *Angewandte Chemie International Edition* **59**, 4099-4105, doi:10.1002/anie.201914000 (2020).
36 Zhang, H. *et al.* Phase segregation due to ion migration in all-inorganic mixed-halide perovskite nanocrystals. *Nature Communications* **10**, 1088, doi:10.1038/s41467-019-09047-7 (2019).
37 Flora, S. J. S. & Pachauri, V. Chelation in metal intoxication. *Int J Environ Res Public Health* **7**, 2745-2788, doi:10.3390/ijerph7072745 (2010).
38 Ferrero, M. E. Rationale for the Successful Management of EDTA Chelation Therapy in Human Burden by Toxic Metals. *Biomed Res Int* **2016**, 8274504-8274504, doi:10.1155/2016/8274504 (2016).
39 Mah, V. & Jalilehvand, F. Lead(II) Complex Formation with Glutathione. *Inorganic Chemistry* **51**, 6285-6298, doi:10.1021/ic300496t (2012).
40 Hayes, J. D. & Pulford, D. J. The Glutathione S-Transferase Supergene Family: Regulation of GST and the Contribution of the Isoenzymes to Cancer Chemoprotection and Drug Resistance Part I. *Critical Reviews in Biochemistry and Molecular Biology* **30**, 445-520, doi:10.3109/10409239509083491 (1995).

41 Zhao, Q. *et al.* Size-Dependent Lattice Structure and Confinement Properties in CsPbI3 Perovskite Nanocrystals: Negative Surface Energy for Stabilisation. *ACS Energy Letters* **5**, 238-247, doi:10.1021/acsenergylett.9b02395 (2020).
42 Noh, J. H., Im, S. H., Heo, J. H., Mandal, T. N. & Seok, S. I. Chemical Management for Colorful, Efficient, and Stable Inorganic–Organic Hybrid Nanostructured Solar Cells. *Nano Letters* **13**, 1764-1769, doi:10.1021/nl400349b (2013).
43 Richter, J. M. *et al.* Ultrafast carrier thermalisation in lead iodide perovskite probed with two-dimensional electronic spectroscopy. *Nature Communications* **8**, 376, doi:10.1038/s41467-017-00546-z (2017).
44 Sun, Q. *et al.* Bright, multicoloured light-emitting diodes based on quantum dots. *Nature Photonics* **1**, 717-722, doi:10.1038/nphoton.2007.226 (2007).
45 Auer-Berger, M. *et al.* All-solution-processed multilayer polymer/dendrimer light emitting diodes. *Organic Electronics* **35**, 164-170, doi:10.1016/j.orgel.2016.04.044 (2016).
46 Yan, F. *et al.* Highly Efficient Visible Colloidal Lead-Halide Perovskite Nanocrystal Light-Emitting Diodes. *Nano Letters* **18**, 3157-3164, doi:10.1021/acs.nanolett.8b00789 (2018).
47 Richter, J. M. *et al.* Enhancing photoluminescence yields in lead halide perovskites by photon recycling and light outcoupling. *Nature Communications* **7**, 13941, doi:10.1038/ncomms13941 (2016).
48 Cho, C. *et al.* The role of photon recycling in perovskite light-emitting diodes. *Nature Communications* **11**, 611, doi:10.1038/s41467-020-14401-1 (2020).
49 Bodnarchuk, M. I. *et al.* Rationalising and Controlling the Surface Structure and Electronic Passivation of Cesium Lead Halide Nanocrystals. *ACS Energy Letters* **4**, 63-74, doi:10.1021/acsenergylett.8b01669 (2019).